Journal of Materials Chemistry A

Accepted Manuscript

ROYAL SOCIETY OF CHEMISTRY

www.rsc.org/materialsA

Valence band engineering and thermoelectric performance optimizing in SnTe by Mn-alloying via zone-melting method

Jun He,[a,b] Xiaojian Tan,[a] Jingtao Xu,*[a] Guo-Qiang Liu,*[a] Hezhu Shao,[a] Yajie Fu,[a] Xue Wang,[a] Zhu Liu,[a] Jiaqiang Xu,[b] Haochuan Jiang,[a] and Jun Jiang,*[a]

Tin telluride (SnTe) has recently attracted lots of interest for its potential thermoelectric application as a lead-free rock-salt analogue of PbTe. However, pristine SnTe samples have high hole concentration due to the presence of intrinsic Sn vacancies, and shows low Seebeck coefficient and high electrical thermal conductivity, resulting in poor thermoelectric performance. In this report, we show that zone-melted SnTe systems with additional Mn (1 - 7 mol %) can control the hole concentration by reducing the Sn vacancies, and modulate the electronic band structure by increasing the band gap and decreasing the energy separation between the light and heavy hole valence bands. Therefore, alloying with additional Mn enhances the contribution of the heavy hole valence band and significantly improves the Seebeck coefficient in $SnMn_xTe$ with the highest value of $\sim 270\ \mu V\ K^{-1}$. A record power factor of 31.9 $\mu W\ cm^{-1}K^{-2}$ has been obtained at 820 K. The maximum thermoelectric figure of merit ZT of $\sim$ 1.25 is found at 920 K in the high quality crystalline ingot of p-type $SnMn_{0.07}Te$.

1 Introduction

Thermoelectric materials, which convert waste heat into useful electrical energy, can lead to more efficient utilization of traditional energies.[1–3] This kind of materials needs a high dimensionless thermoelectric figure of merit defined as $ZT = \sigma S^2 T/\kappa$, where σ is electrical conductivity, S is the Seebeck coefficient, κ is thermal conductivity, and T is the absolute temperature. The thermal conductivity contains two parts: the electronic contribution κ_e and the lattice contribution κ_{lat}. To optimize thermoelectric performance, one should increase the power factor $S^2\sigma$ and/or reduce the lattice contribution to the thermal conductivity. The reduction of the lattice thermal conductivity κ_{lat} has been achieved through phonon scattering by point defects, grain boundaries, and intrinsic anharmonic phonons.[4–7] The approaches that can improve the power factor include the manipulation of the density of states via band engineering through the introduction of resonant impurity states near the Fermi level[8,9] or convergence of degenerate electronic bands by alloying[10,11].

It has been found that lead telluride (PbTe) and its alloys have the best thermoelectric performance in the middle temperature range. Solid solution alloying with Mg, Mn increases the band gap of PbTe and decreases the energy difference between the light (L point) and heavy (Σ point) valence bands so the control of band convergence with respect to temperature can be improved.[12–14] Second phase nanostructuring with PbS or SrTe has significantly enhanced the thermoelectric performance giving rise to a maximum ZT value of $\sim$ 2.3.[15,16] However, the applications of PbTe-based alloys have been limited because of the environmental concern regarding Pb. Tin telluride (SnTe), a lead-free compound whose crystalline and band structures are similar to PbTe, has not received much attention as a promising thermoelectric material until these years. One reason is that the very high carrier concentration resulting from the intrinsic Sn vacancies leads to a low Seebeck coefficient and a high electrical thermal conductivity κ_e.[17–19] Another undesirable feature is that SnTe has a smaller band gap (about 0.18 eV at 300 K) and a larger energy separation (0.35 eV at 300 K) between the light hole valence band at L point and heavy hole valence band at Σ point when compared to PbTe (0.30 eV and 0.17 eV at 300 K, respectively.)[17–19]

The prospect of alloying SnTe with other telluride such as AgSbTe and $AgBiTe_2$ to enhance its thermoelectric performance has been explored[20,21]. Doping SnTe with In has been reported to give rise to resonant states in the valence band and cause a significant enhancement of the Seebeck coefficient, which results in a ZT of $\sim$ 1.1 at 873 K.[9] Similar phenomena has been reported in $SnTe_{1-x}Se_x$:In, where the reduction of κ_{lat} has been achieved by Se doping.[22] The compensation effect by extra cations, such as Sn or Pb, has been reported to have the significant effect of reducing the Sn vacancies and effectively decreasing the hole carrier density, improving the ZT by $\sim 50\%$[23,24]. The carrier concentration of SnTe has also been tuned effectively via I doping to affect the thermoelectric properties.[25] Recent studies of Cd, Hg, Mg alloying in SnTe have show that the band engineering, which can greatly enhances the Seebeck coefficient, is an efficient way to achieve high ZT values of over 1.2[23,26–28].

Mn has been alloyed with PbTe to modify the band structure which successfully enhanced the thermoelectric perfor-

[a]*Ningbo Institute of Materials Technology and Engineering, Chinese Academy of Science, Ningbo 315201, China. Fax: +86-574-86688067; Tel: +86-574-86688067; E-mail: xujingtao@nimte.ac.cn, liugq@nimte.ac.cn, jjun@nimte.ac.cn*

[b]*NEST Lab, Department of Chemistry, College of Sciences, Shanghai University, Shanghai 200444, P.R. China*

mance of the PbTe.[13,14] Similar band engineering by Mn alloying is also expected in SnTe to increase the band gap and decrease the energy difference between the light and heavy valence bands, which will facilitate the convergence of the valence band valleys, leading to an optimised thermoelectric performance. In this paper, we report the effect of additional Mn alloying on the electronic structure and the thermoelectric performance of SnTe. The $SnMn_xTe$ alloys (x = 0, 0.01, 0.03, 0.05, 0.07) are synthesized by a zone-melting method.[24] Alloying with additional Mn suppresses the Sn vacancies and reduces the hole concentration. Besides, Mn alloying tunes the electronic band structure of SnTe by decreasing the energy difference between the light and heavy hole valence bands, leading to a significant enhancement of the Seebeck coefficient. As a result, the p-type $SnMn_{0.07}Te$ sample shows a maximum ZT of $\sim$ 1.25 at $\sim$ 920 K. Our finding suggests that SnTe-based materials have great potential for thermoelectric power generation and deserve further investigations.

2 Experimental

Reagents. Tin (99.999+ %), tellurium (99.999+ %), and manganese (99.99+ %) were used for synthesis without further purification.

Synthesis. The $SnMn_xTe$ (x = 0, 0.01, 0.03, 0.05, and 0.07) samples were synthesized by mixing appropriate ratios of high purity starting materials Mn, Sn and Te in a sealed quartz ampoule with an inner diameter 10 mm in a vacuum with pressure below 10^{-2} Pa). The ampoules were slowly heated to 1123 K within 6 hours, and soaked at this temperature for 2 hours in a rocking furnace to ensure the homogeneity of composition, and then cooled to room temperature in the air. These samples were grown in a zone-melting furnace at 1123 K with a speed of 25 mm h^{-1}. Only the middle parts of the zone-melting samples were used for subsequent analysis.

Powder X-ray Diffraction. The phase compositions of the prepared samples were determined by the powder X-ray diffraction (XRD) analysis using the Cu K_α radiation (λ = 1.5406 Å).

Electrical Transport. The electrical conductivity and Seebeck coefficient were measured by the thermoelectric measurement system (ZEM-3 ULVAC, Japan) in a low-pressure helium atmosphere from room temperature to 920 K. The typical sample shape used in the measurement is a bar of size $\sim$ $10\times2\times2$ mm^3.

Hall Measurement. The carrier concentration n and mobility μ were calculated from the Hall coefficient (R_H) measured using the physical properties measurement system (PPMS, Quantum Design) in a magnetic field ranging from 0 to 5 T.

Thermal Conductivity. The thermal conductivity was calculated from the values of the thermal diffusivity D, the density ρ and the specific heat C_p via the relation $\kappa = D\rho C_p$. D was measured by a laser flash system (Netzsch, LFA-457, Germany) on the plate of $\phi10\times2$ mm^2. During the measurements, the samples were coated with a thin layer of graphite to minimize errors due to the emissivity of the materials. The heat capacity can be obtained by $C_p = C_{p,300} + C_{p1} \times ((T / 300)^\alpha - 1) / ((T / 300)^\alpha + C_{p1}/C_{p,300})$[29], where $C_{p,300}$ is the specific heat capacity at 300 K. ρ of zone-melted $SnMnxTe$ alloys was determined using the Archimedes principle (as shown in Table S1, Supporting Information).

Computational Details. The first-principles calculations are performed using a plan-wave pseudopotential formulation within the framework of the density functional theory (DFT)[30–32] as implemented in the VASP package. The electron-ion interaction is modeled using the projector-augmented wave (PAW) technique[33,34]. The energy cutoff is set as 500 eV. The exchange-correlation energy is expressed the Perdew-Burke-Ernzerhof (PBE) form[35] with generalized gradient approximation (GGA). The potentials for Sn, Te, and Mn contain the $5s^25p^2$, $5s^25p^4$, and $3d^54s^2$ electrons as valence electrons respectively. The doped SnTe is modeled by a 3 × 3 × 3 supercell which contains 27 Sn atoms and 27 Te atoms. The Brillouin zone is sampled with 4 × 4 × 4 Monkhorst-Pack k meshes. During the geometry optimization, both the lattice constant and atomic positions are fully relaxed until the force acting on all atoms becomes less than 0.02 eV/Å. Since the Te atom is a heavy element, the effect of spin-orbit (SO) coupling is included in our calculations.

3 Results and discussion

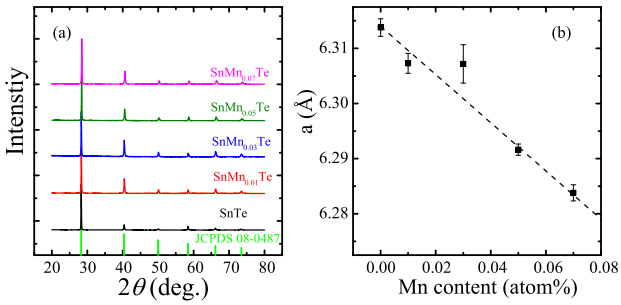

Fig. 1 (Color online) (a) X-ray diffraction patterns of $SnMn_xTe$ samples. (b) The lattice parameter as a function of Mn content. The dashed line indicates the Vegard's law for the solid solution of SnTe and MnTe.

$SnMn_xTe$ (x = 0, 0.01, 0.03, 0.05, 0.07) samples were synthesized by a zone-melting method and characterized by powder X-ray diffraction. As shown in Fig. 1(a) the XRD patterns could be indexed on the cubic SnTe structure ($Fm\bar{3}m$ space group) with no other impurity phase up to the detection limit

of powder XRD. The lattice parameter were calculated according to the XRD patterns and shown in Fig. 1(b). The lattice parameter decreases linearly with increasing the Mn amount, which is consistent with the fact that MnTe has a smaller lattice parameter (5.875 Å) than SnTe (6.314 Å)[36], and obeys the Vegard's law of solid solution.

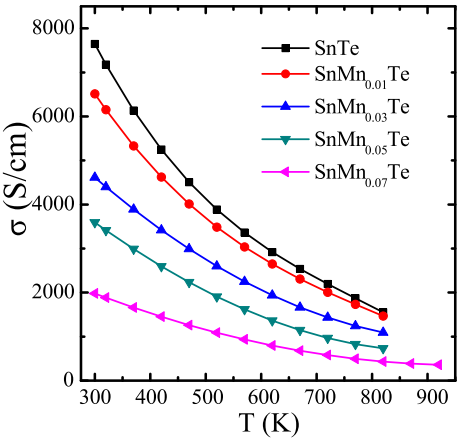

Fig. 2 (Color online) Electrical conductivity as a function of temperature for $SnMn_xTe$ samples.

The temperature dependent electrical conductivity is shown in Fig. 2. For all samples, the electrical conductivity decreases with as temperature increases, which is the typical behavior of degenerate semiconductors. The electrical conductivity (Fig. 2(a)) decreases with increasing Mn concentration . The room temperature electrical conductivity decreases from $\sim$ 7600 S cm^{-1} for pristine SnTe to $\sim$ 2000 S cm^{-1} for $SnMn_{0.07}Te$. The Hall coefficient R_H of all $SnMn_xTe$ (x = 0-0.07) samples are positive at room temperature, so the hole carriers dominate the electrical conduction. The room temperature carrier concentration and Hall mobility are listed in Table 1. The carrier concentration increases when a small amount of Mn is introduced at x = 0.01. The introduction of additional Mn results in decreasing carrier concentration, which suggests that the Sn vacancies are reduced by additional Mn. The carrier concentration of the $SnMn_xTe$ samples only decreases to 3.15 $\times$ 10^{20} cm^{-3}. Additional Mn is much less efficient in reducing carrier concentration than Sn-self compensation ($\sim$ 2 $\times$ 10^{20} cm^{-3} for $Sn_{1.03}Te$) or additional Pb (2.16 $\times$ 10^{20} cm^{-3} for $SnPb_{0.04}Te$).[23,24] According to previous reports,[9,22,23,27,28] SnTe-based materials show best thermoelectric performance when the carrier concentration is lower than 2.5 $\times$ 10^{20} cm^{-3}. To further decrease the carrier concentration, $SnMn_{0.09}Te$ was grown by zone-melting, but shows very poor quality with lots of pores, leading to unreliable data. The samples with higher Mn concentration may be obtained by other synthesis method, such as hot-pressing or spark plasma sintering.

Normally, the mobility changes in a way that is opposite to the carrier concentration due to the electron-electron interaction. Therefore, an increase of the Hall mobility is expected, as the carrier concentration decreases with additional Mn. However, the Mn alloyed samples show smaller mobilities than pristine SnTe. This suggests that additional Mn atoms induces very strong scattering of the carriers.

Table 1 The hole concentration n, Hall mobility μ, and effective mass m^* of $SnMn_xTe$ samples.

sample	n (10^{20} cm^{-3})	μ (cm^2 V^{-1}s^{-1})	m^* (m_0)
SnTe	5.76	82.9	1.24
$SnMn_{0.01}Te$	8.01	50.8	1.53
$SnMn_{0.03}Te$	5.94	48.6	1.13
$SnMn_{0.05}Te$	3.15	71.2	0.81
$SnMn_{0.07}Te$	3.28	37.7	1.09

The temperature dependence of the Seebeck coefficient of $SnMn_xTe$ samples are shown in Fig. 3(a). The positive values of the Seebeeck coefficient are consistent with the Hall coefficient measurements. For all samples, the Seebeck coefficient increases with temperature, and does not saturate until 920 K. As the amount of Mn increases, the room temperature Seebeck coefficient first decreases from $\sim$ 40 μV K^{-1} for pristine SnTe to $\sim$ 35 μV K^{-1} for $SnMn_{0.03}Te$, and then increases significantly to $\sim$ 50 μV K^{-1} for $SnMn_{0.07}Te$. The Seebeck coefficient at high temperature (820 K) increases with the Mn amount from $\sim$ 130 μV K^{-1} for pristine SnTe to $\sim$ 225 μV K^{-1} for $SnMn_{0.07}Te$. For $SnMn_{0.05}Te$ and $SnMn_{0.07}Te$, the Seebeck coefficient increases linearly with temperature. For $SnMn_{0.07}Te$, the Seebeck coefficient at 920 K is $\sim$ 270 μV K^{-1}, which is the highest value reported so far in the SnTe-based alloys.

The effective mass is roughly estimated based on a single band assumption, although for SnTe two valence bands contribute to the conduction. The results are listed in Table 1. It is noticeable that for $SnMn_{0.05}Te$ and $SnMn_{0.07}Te$ whose carrier concentration is around 3 $\times$ 10^{20} cm^{-3}, the effective mass does not decrease greatly and remains to be $\sim$ 1.0 m_e. This result suggests that the heavy hole valence band may still have great contribution at this carrier concentration. To clarify this point, the room temperature Seebeck coefficients of $SnMn_xTe$ samples are plotted versus carrier concentration in Fig. 3(b). The previously reported experimental data of In doped SnTe,[9] In doped $SnTe_{0.85}Se_{0.15}$,[22] Cd doped SnTe,[23] Hg doped SnTe,[27] Cd/In co-doped SnTe,[28] Cu doped SnTe,[19] Pb alloyed SnTe,[24] and the theoretical S vs n curve[9] are also present for comparison. As shown in the Fig. 3(b), the Seebeck coefficients of In and Cd/Hg/Mg doped SnTe samples are above the theoretical Pisarenko cure, showing great en-

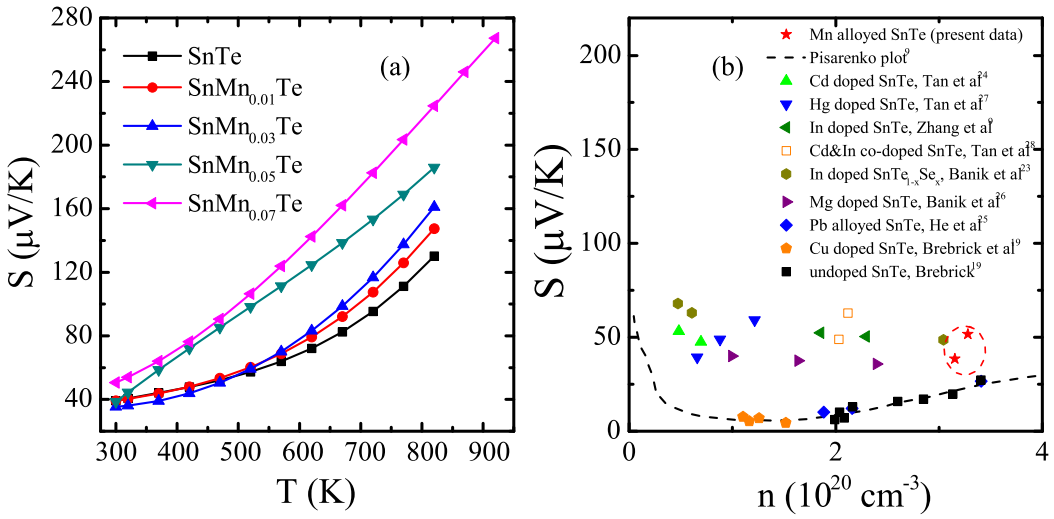

Fig. 3 (Color online) (a) The temperature dependence of the Seebeck coefficient of $SnMn_xTe$ samples. (b) Room temperature S vs n plot of the present $SnMn_xTe$ samples. Previously reported S vs n data of undoped SnTe,[19], Cd doped SnTe,[23] Hg doped SnTe,[27] In, Cd co-doped SnTe, In doped SnTe.[9], In doped $SnTe_{0.85}Se_{0.15}$,[22] Cu doped SnTe,[19] Pb alloyed SnTe,[24] and theoretical Pisarenko curve based on VBM model[9] are also plotted in b for comparison.

hancement due to formation of resonant levels[9] and valence band convergence[23,26,27], respectively. It is clearly observed that $SnMn_xTe$ samples also have significantly larger Seebeck coefficients than the theoretical prediction of Pisarenko curve.

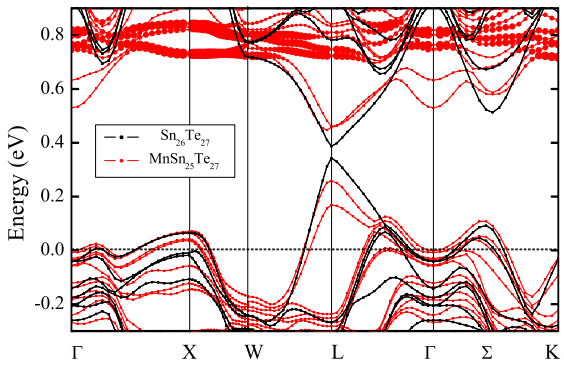

Fig. 4 (Color online) Calculated band structures for $Sn_{26}Te_{27}$ (black line) and $MnSn_{25}Te_{27}$ (red line) with SO coupling. The character weight of Mn-d electrons is represented by the size of the red filled circles. The Fermi level is at 0 eV.

To understand the origin of the enhancement of the Seebeck coefficient, we have performed DFT calculation of the electronic structure of pristine SnTe and Mn-doped SnTe. Previous reports have shown that the Sn vacancies (V_{Sn}) have negative formation energy regardless the growth condition.[37] Our experimental results show that the hole concentration of $SnMn_xTe$ ($x = 0$ - 0.07) samples is still at the level of 3×10^{20} cm^{-3}. Therefore, it is reasonable to include some Sn vacancy in the DFT calculation. For the case with both Sn vacancy and doped Mn atoms, there are multiple V_{Sn}-Mn_{Sn} arrangements which should be created in the supercell. We calculated V_{Sn}-Mn_{Sn} defect pairs with the largest distance (7.846 Å) in the supercell.

As can be seen in Fig 4, the energy separation between the light-hole valence band (at L-point) and the heavy-hole valence band (near Σ-point) $\Delta E_{L-\Sigma}$ (0.15 eV) is reduced relative to that in pristine SnTe (0.25 eV). The reduction of $\Delta E_{L-\Sigma}$ indicates a degenerate multiple valence bands effect, leading to enhanced Seebeck coefficient. Moreover, the band gap E_g of SnTe is enlarged from 0.04 to 0.15 eV with Mn doping. In PbTe, the similar valence band engineering has been experimentally observed.[14] Recent theoretical study indicated that the band tuning is due to the anti-bonding of Mn-d and Te-p obitals.[14] This kind of band gap enlargement could increase the Seebeck coefficient and suppress the bipolar diffusion, and these two aspects are both beneficial to the thermoelectric properties.

The energy separation between the light and heavy hole valence bands significantly decreases from 0.25 eV in pristine samples to 0.15eV in 4 mol % Mn alloyed SnTe samples. Thus, adding Mn in SnTe results in improvement of the valence band degeneracy, which is expected to enhance the Seebeck coefficient due to contributions from both bands because there is an asymmetric increase in the density of states near

the Fermi level. Similar phenomena have been reported in Cd/Hg/Mg doped SnTe[23,26,27] and Cd/Mg/Mn doped PbTe.[13]

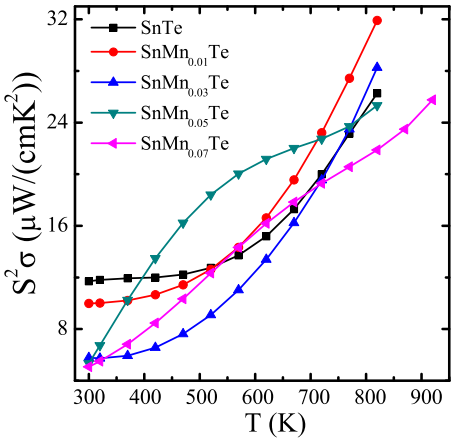

Fig. 5 (Color online) The temperature dependence of power factors ($S^2\sigma$) of $SnMn_xTe$ samples.

The power factor data of $SnMn_xTe$ (x = 0-0.07) samples are plotted in Fig. 5 as a function of temperature. With the increase of the Mn content, the power factor at room temperature decreases from 11.7 μW cm^{-1}K^{-2} for pristine SnTe to 5.0 μW cm^{-1}K^{-2} for $SnMn_{0.07}Te$, mainly due to the decrease of the electrical conductivity. The high temperature values (at 820 K) increases in $SnMn_{0.01}Te$ due to the enhanced Seebeck coefficient, but then decreases with x due to the decrease of the electrical conductivity. The highest power factor obtained in $SnMn_{0.01}Te$ is 31.9 μW cm^{-1}K^{-2} at 820 K, which is indeed higher than those of the previously studied SnTe-based alloys.[24]

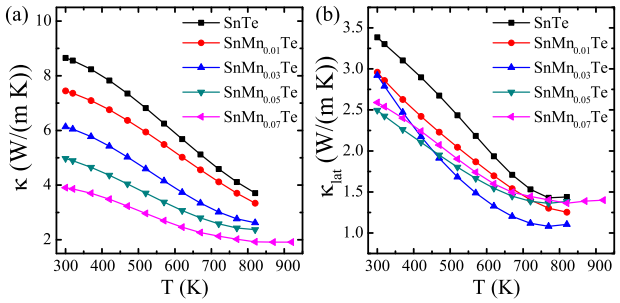

Fig. 6 (Color online) The temperature dependence of (a) total thermal conductivity and (b) lattice thermal conductivity of $SnMn_xTe$ samples.

The temperature dependences of total thermal conductivity and lattice thermal conductivity of $SnMn_xTe$ samples are shown in Fig. 6. The room temperature thermal conductivity decreases with x from 8.6 W m^{-1}K^{-1} for pristine SnTe to $\sim$ 4 W m^{-1}K^{-1} for $SnMn_{0.07}Te$. The lattice thermal conductivities are calculated by subtracting the electronic contribution from the total thermal conductivities. The electronic contribution is computed using the Wiedemann-Franz law: $\kappa_e = L\sigma T$, where L is the Lorenz number. Here, the L value (Figure S2, Supporting Information) is obtained from the well-established approach of fitting the Seebeck data to the reduced chemical potential.[38–40] As shown in Fig. 6(b), the lattice thermal conductivity of Mn alloyed SnTe samples is suppressed compared to pristine SnTe. But no definitive dependence between κ_{lat} and x can be observed. The optimization of total thermal conductivity is mainly due to the control of electrical conductivity (see Figure S3, Supporting Information). Similar phenomena have been observed in Cd doped SnTe, Mg doped SnTe, and Pb alloyed SnTe.[23,24,26] The lowest lattice thermal conductivity at high temperatures (820 K to 920 K) is still within the range of 1.0 - 1.5 W m^{-1}K^{-1}.

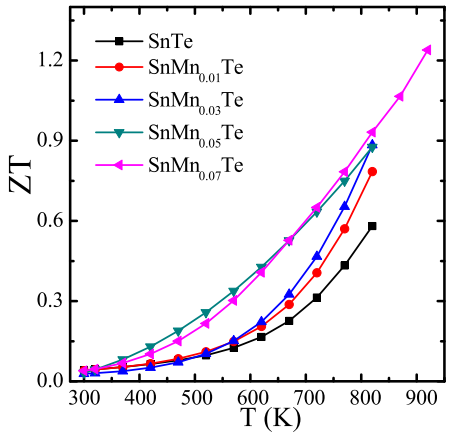

Fig. 7 (Color online) The temperature dependence of ZTs of $SnMn_xTe$ samples.

The temperature dependent ZT values of the $SnMn_xTe$ (x = 0-0.07) samples are presented in Fig. 7. The ZTs at high temperatures increases with the Mn amount. The highest ZT of $\sim$ 1.25 is obtained in $SnMn_{0.07}Te$ at 920 K, due to the significantly enhanced Seebeck coefficient and the reduced thermal conductivity. The highest ZT obtained in the present alloys synthesized by the commercial zone-melting method is comparable to previously reported maximum ZT of spark plasma sintered Cd doped ($\sim$ 1.3 at 873 K), Hg doped ($\sim$ 1.35 at 910 K), In doped ($\sim$ 1.1 at 873 K), and Cd/In co-doped ($\sim$ 1.4 at 923 K) SnTe samples.[9,23,27,28] As the lattice thermal conductivity is still over 1 W m^{-1}K^{-1}, the ZT may be further improved by decreasing κ_{lat} via nanostructuring [23,27,28] or alloying[22].

4 Conclusions

The poor thermoelectric performance of pristine SnTe can be improved by tuning the carrier concentration and modifying the band structure. Mn alloyed samples $SnMn_xTe$ have larger band gap and smaller energy separation between the light (L point) and heavy (Σ point) valence bands than pristine SnTe. Therefore, effective convergence of two valence bands gives rise to significant enhancement of the Seebeck coefficient of $SnMn_xTe$ (x = 0.05, 0.07). This type of band engineering is a crucial finding of this work as it leads to a high figure of merit in $SnMn_{0.07}Te$ ($ZT \sim 1.25$ at 920 K). The thermoelectric performance of SnTe may be further improved through phonon engineering by alloying or nanostructuring, so it may serve as an efficient lead-free alternative to lead chalcogenides in high temperature power generation applications in the near future.

5 Acknowledgements

This work is supported by the National Nature Science Foundation of China (NSFC No. 11304327, 11404348, 11404350, and 11234012), Ningbo Municipal Natural Science Foundation (2015A610031, 2014A610011), and Ningbo Science and Technology Innovation Team (Grant No. 2014B82004).

References

1 Bell, L. E. Science, 200, **321**, 1457.
2 DiSalvo, F. J. Science, 1999, **285**, 703.
3 Snyder, G. J.; Toberer, E. S. Nat. Mater., 2008, **7**, 105.
4 Sootsman, J. R.; Chung, D. Y.; Kanatzidis, M. G. Angew. Chem., Int. Ed., 2009, **48**, 8616.
5 Kanatzidis, M. G. Chem. Mater., 2010, **22**, 648.
6 Delaire, O.; Ma, J.; Marty, K.; May, A. F.; McGuire, M. A.; Du, M.-H.; Singh, D.J.; Podlesnyak, A.; Ehlers, G.; Lumsden, M.D.; Sales, B. C. Nat. Mater., 2011, **10** 614.
7 Suekuni, K.; Avila, M. A.; Umeo, K.; Fukuoka, H.; Yamanaka, S.; Nakagawa, T.; Takabatake, T. Phys. Rev. B, 2008, **77**, 235119.
8 Heremans, J. P.; Jovovic, V.; Toberer, E. S.; Saramat, A.; Kurosaki, K.; Charoenphakdee, A.; Yamanaka, S.; Snyder, G. J. Science, 2008, **321**, 554.
9 Zhang, Q.; Liao, B.; Lan, Y.; Lukas, K.; Liu, W.; Esfarjani, K.; Opeil, C.; Broido, D.; Chen G.; Ren, Z. Proceedings of the National Academy of Sciences, 2013, **110**, 13261).
10 Pei, Y. Z.; Shi, X.; LaLonde, A.; Wang, H.; Chen, L. D.; Snyder, G. J. Nature, 2011, **473**, 66.
11 Liu, W.; Tan, X. J.; Yin, K.; Liu, H.; Tang, X. F.; Shi, J.; Zhang, Q. J.; Uher, C. Phys. Rev. Lett., 2012, **108**, 166601.
12 Zhao, L.-D.; Wu, H. J.; Hao, S. Q.; Wu, C. I.; Zhou, X. Y.; Biswas, K.; He, J. Q.; Hogan, T. P.; Uher, C.; Wolverton, C.; Dravid, V. P.; Kanatzidis, M. G. Energy Environ. Sci., 2013, **6**, 3346.
13 Pei, Y. Z.; Wang, H.; Gibbs, Z. M.; LaLonde, A.D.; Snyder, G.J. NGP Asia Materials, 2012, **4**, e28.
14 Tan, X. J.; Shao, H. Z.; Hu, T. Q.; Liu G.-Q.; Ren, S.-F. J. Phys: Condens. Matter, 2015, **27** 095501.
15 Wu, D.; Zhao, L.-D.; Tong, X.; Li, W.; Wu, L. J.; Tan, Q.; Pei, Y. L; Huang, L.; Li, J.-F.; Zhu, Y. M.; Kanatzidis, M.G.; He, J. Q. Energy & Enviromental Science, 2015, **8**, 2056.
16 Biswas, K.; He, J.; Blum, I. D.; Wu, C. I.; Hogan, T. P.; Seidman, D. N.; Dravid, V. P.; Kanatzidis, M. G. Nature, 2012, **489**, 414.
17 Brebrick, R. F. J. Phys. Chem. Solids, 1963, **24**, 27.
18 Rogers, L. M. J. Phys. D: Appl. Phys., 1968, **1**, 845).
19 Brebrick, R. F.; Strauss, A. J. Phys. Rev., 1963, **131**, 104.
20 Chen, Y.; Nielsen, M. D.; Gao, Y. B.; Zhu, T. J.; Zhao, X.; Heremans, J. P. Advanced Energy Materials, 2012, **2**, 58.
21 Tan, G.; Shi, F.; Sun, H.; Zhao, L.-D.; Uher, C.; Dravid V. P.; Kanatzidis, M. G. Journal of Materials Chemistry A, 2014, **2**, 20849.
22 Banik, A.; Biswas, K. J. Mater. Chem. A, 2014, **2**, 9620.
23 Tan, G.J.; Zhao, L.-D.; Shi, F.; Doak, J. W.; Lo, S.-H.; Sun, H.; Wolverton, C.; Dravid, V. P.; Uher, C.; Kanatzidis, M. G. Journal of the American Chemical Society, 2014, **136**, 7006.
24 He, J.; Xu, J. T.; Liu, G. Q.; Tan, X. J.; Shao, H. Z.; Xu, J. Q.; Jiang, J.; Jiang, H. C. RSC Adv., 2015, **5**, 59379.
25 Zhou, M.; Gibbs, Z. M.; Wang, H.; Han, Y. M.; Xin, C. N.; Li, L.F.; Snyder, G. J. Phys. Chem. Chem. Phys., 2014 **16**, 20741.
26 Banik, A.; Shenoy, U. S.; Anand, S.; Waghmare, U. V.; Biswas, K. Chem. Mater., 2015, **27**, 581.
27 Tan, G. J.; Shi, F. Y.; Doak, J. W.; Sun, H.; Zhao, L.-D.; Wang, P.; Uher, C.; Wolverton, C.; DravidV. P.; Kanatzidis, M. G. Energy & Environmental Science, 2015, **8**, 267.
28 Tan, G. J.; Shi, F. Y.; Hao, S. Q.; Chi, H.; Zhao, L.-D.; Uher, C.; Wolverton, C.; Dravid, Y. P.; Kanatzidis, M. G. Journal of the American Chemical Society, 2015, **137**, 5100.
29 Wagner, M. These de doctorat, Universität Wien, 2007.
30 Kresse, G.; Hafner, J. Phys. Rev. B, 1993, **47**, R558.
31 Kresse, G.; Hafner, J. Phys. Rev. B, 1994, **49**, 14251.
32 Kresse G.; Furthmüller, J. Comput. Mater. Sci., 1996, **6**, 15.
33 Blöchl, P. E. Phys. Rev. B, 1994, **50**, 17953.

34 Kresse, G.; Joubert, D. Phys. Rev. B, 1999 **59**, 1758.
35 Perdew, J.P.; Burke, K.; Ernzerhof, M. Phys. Rev. Lett., 1996, **77**, 3865.
36 Leung, C.-H.; VanVlack, L. H. Journal of the American Ceramic Society, 1979, **62**, 613.
37 Wang, N.; West, D.; Liu, J.; Li, J.; Yan, Q.; Gu, B.-L.; Zhang, S.; Duan, W. Physical Review B, 2014, **89**, 045142.
38 Johnsen, S.; He, J.; Androulakis, J.; Dravid, V. P.; Todorov, I.; Chung, D. Y.; Kanatzidis, M. G. J. Am. Chem. Soc, 2011, **133**, 3460.
39 May, A. F.; Fleurial, J.-P.; Snyder, G. J. Phys. Rev. B, 2008, **78**, 125205.
40 Girard, S. N.; He, J.; Zhou, X.; Shoemaker, D.; Jaworski, C. M.; Uher, C.; Dravid, V. P.; Heremans, J. P.; Kanatzidis, M. G. J. Am. Chem. Soc., 2011, **133**, 16588.